

Composition and Dynamics of the Planetary Boundary Layer in Cold and Dark Atmospheres: Meteorological Overview from the ALPACA-2022 Field Experiment

Gilberto J. Fochesatto^a, Kathy S. Law^b, Julia Schmale^c, Stefano Decesari^d, William R. Simpson^e, Roman Pohorsky^c, Brice Barret^f, Andrea Baccarini^c, Elsa Dieudonné^g, Natalie Brett^b, Robert Gilliam^h, Douglas Kellⁱ, Antonio Donateo^j, Gianluca Pappaccogli^j, Federico Scoto^j, Maurizio Busetto^d, Sarah Albertin^k, Slimane Bekki^b, Francois Ravetta^b, Jean-Christophe Raut^b, Cristelle Cailteau-Fischbach^b, Meeta Cesler-Malone^e, Jingqiu Mao^e, Steve Arnold^l, Brice Temime-Roussel^m, Barbara D'Anna^m, Joel Savarino^k, Julia Maillard^b, Eleftherios Ioannidis^b, Konstantinos Doulgerisⁿ, David Brusⁿ, David Atkinson^o, Eric Petersen^p, Hiroki Iwata^q, Masahito Ueyama^{r,s}, Yoshinubo Harazono^{r,s}.

- (a) Department of Atmospheric Sciences, University of Alaska Fairbanks, Fairbanks, Alaska USA 99775.
- (b) Sorbonne Université, UVSQ, CNRS, LATMOS, 75252 Paris, France
- (c) Extreme Environments Research Laboratory. Ecole Polytechnique Fédérale de Lausanne, Route des Ronquos 86, 1950 Sion, Switzerland
- (d) CNR-ISAC, National Research Council of Italy, Institute of Atmospheric Sciences and Climate, Via Gobetti 101, Bologna, IT 40129, Italy
- (e) Department of Chemistry. University of Alaska Fairbanks, Fairbanks, Alaska. USA 99775
- (f) Laboratoire d'Aérologie (LAERO), Université Toulouse III – Paul Sabatier, CNRS, Toulouse, France
- (g) Laboratoire de Physico-Chimie de l'Atmosphère, Université du Littoral Côte d'Opale, Dunkerque, France.
- (h) Environmental Protection Agency, USA
- (i) Laboratoire de Météorologie Dynamique du CNRS Ecole Polytechnique. Palaiseau, France.
- (j) National Research Council of Italy, Institute of Atmospheric Sciences and Climate (CNR-ISAC), Lecce, Italy
- (k) Univ. Grenoble Alpes, CNRS, Institut des Géosciences de l'Environnement (IGE), UMR 5001, Grenoble 38041, France.
- (l). School of Earth and Environment, University of Leeds, Leeds, LS2 9JT, UK
- (m) Aix-Marseille Université - Campus Marseille Centre, Bâtiment de Chimie, 3 Place Victor Hugo, Marseille, 13003.
- (n). Finnish Meteorological Institute, Helsinki, Finland.
- (o). Department of Geography. University of Victoria, Victoria Canada.
- (p) Geophysical Institute. University of Alaska Fairbanks. Fairbanks, USA 99775.
- (q) Department of Environmental Science, Faculty of Science, Shinshu University, Matsumoto, Japan
- (r) Graduate School of Agriculture, Osaka Metropolitan University, Sakai, Japan.
- (s) International Arctic Research Center, University of Alaska Fairbanks, Fairbanks, USA 99775.

Corresponding author: Javier Fochesatto, gjfochesatto@alaska.edu

ABSTRACT

In the polar regions, the extreme cold and dark atmosphere of the winter season imposes stringent conditions on the planetary boundary-layer (PBL) leading to limited vertical atmospheric mixing and increasing the severity of air pollution episodes. Understanding the physical and chemical transformations affecting air pollution critically depends on our ability to accurately describe the dynamics of the planetary boundary layer (PBL). This requires an adequate combination of modeling, ground-based observations, and vertical profile measurement systems to assess emission dispersion and transport in stratified environments. The science of Alaskan Layered Pollution And Chemical Analysis (ALPACA) centers on improving our understanding of localized winter air pollution in the Arctic.

We present an overview of the meteorological situation and PBL observations collected during the ALPACA field experiment in Fairbanks, Alaska in winter 2022. Surface and vertical profile observations of radiation, turbulence, dynamics, and composition were collected at a site affected by surface and elevated emissions. The study area is the Tanana Valley in the Interior of Alaska, which experiences persistent synoptic anticyclonic conditions resulting in stagnant flow and limited ventilation, exacerbating air pollution levels. These conditions are interspersed with periodic transits of cyclonic air masses influencing the PBL through radiative forcing that erodes low-level temperature inversion layers and mixes local air masses into the free troposphere. This paper highlights the research objectives, experimental findings and first results linking meteorological conditions with the observed structure and composition of the PBL.

SIGNIFICANCE STATEMENT

This article provides an overview of the meteorology during the ALPACA-2022 winter field experiment. It also presents observations designed to better understand the physical processes influencing the planetary boundary layer (PBL) and its role in wintertime Arctic air pollution. It describes the synoptic meteorological conditions throughout the experiment and the diverse range of instrumental platforms used to study the dynamics and composition of the Arctic polluted PBL for the first time. The article emphasizes the importance of multi-instrumental platforms to improve understanding of the PBL composition and dynamics in the context of Arctic air pollution. This is particularly relevant in conditions with limited photochemistry and in areas experiencing very cold, stable

environments that exacerbate pollution levels. The observations are used to improve meteorological and air quality model simulations.

CAPSULE

- Highlights of the PBL dynamics and composition in cold and dark atmospheres.
- High latitude synoptic and surface conditions as drivers of the PBL state.
- Comparison of model results and observations.

1. Introduction

The Alaskan Layered Pollution And Chemical Analysis (ALPACA) project was developed under the International Global Atmospheric Chemistry (IGAC)/International Arctic Science Committee (IASC) Air Pollution in the Arctic: Climate, Environment and Societies (PACES) initiative (Arnold et al. 2016). It was initiated to develop and promote scientific activities aimed at improving the understanding of localized winter air pollution in the Arctic (Schmale et al., 2018). This is a common interest across the international community along with improving numerical predictions of Arctic air quality, planetary boundary layer (PBL) meteorology, and their relationship. In the stable conditions of the cold and dark Arctic winters, dispersion and transformation of emitted pollutants are heavily controlled by meteorological conditions. Under stable wintertime conditions, atmospheric pollutants can be advected from emission regions and accumulate in the Arctic, leading to enhanced background concentrations of trace gases and aerosols characteristic of “Arctic haze” events (Barrie, 1986). Advancing the understanding of these processes requires experimental research that integrates multi-instrument observational platforms with modeling tools, enabling improved characterization of the complex dynamics of the wintertime PBL and associated air pollution patterns. The ALPACA-2022 field experiment focused on these objectives and highlighted the synergy of an integrated, observational approach to gather data to improve our understanding and simulation of aerosols, trace gasses, and boundary layer meteorology in the wintertime Arctic.

The ALPACA project scientific objectives were first summarized by the scientific community in a white paper by Simpson et al. in 2018. This led to the design and planning of a major international field experiment, supported by several large research programs, which took place in Fairbanks, Alaska in January and February 2022. The concept and design of ALPACA-2022 are described in Simpson et al. (2024), with the scientific objectives, social science connections, and some initial results. This companion paper focuses on detailing the meteorological situation during the field campaign, including the climatological context. It also describes, in more detail, the suite of measurements that were made to address specific objectives related to the dynamics and composition of the PBL, and provides some initial highlights from the field campaign. The ALPACA-2022 winter field experiment hypotheses and science goals linked to the PBL dynamics and composition are given in Table 1.

Table 1. ALPACA-2022 winter field experiment goals related to boundary layer dynamics and composition.

Boundary Layer Dynamics - Goals	
G1	Understanding the buildup and breakup of shallow, stratified Surface Based temperature Inversion layers (SBIs) during the stagnant Anticyclonic (AC) synoptic conditions.
G2	Characterizing the PBL behavior, including the SBI and Elevated temperature Inversion (EI) layers during ACs, Transitioning phases (T), and Cyclonic (C) conditions and their radiative coupling and feedback on surface turbulence.
G3	Specifying PBL dynamic and turbulent regimes (vertical, horizontal, and transient) in the presence of Shallow Cold Flows (SCFs), which can control the mixing and transport of aerosols.
Boundary Layer Composition, Aerosols, and Gas Phase - Goals	
G4	Investigating the vertical and horizontal dispersion of aerosols and trace gasses under varying meteorological conditions, including the degree to which power plant emissions affect ground-level air quality.
G5	Determining how well chemical transport models simulate dispersion, composition, and the processing and deposition of air pollution.
G6	Determining the role of snow/air exchange and chemical reactions as a source (emission) and sink (wet and dry deposition) of trace gasses and aerosols.
G7	Investigating the fate of air pollutants, including deposition and potential impacts on the climate when compared to background Arctic haze.

2. Large-Scale Meteorology: PBL Dynamics and Pollution in Wintertime Alaska

Large-scale atmospheric circulation patterns and ocean conditions strongly influence Alaska's continental meteorology (Stone 1997). The strength and position of the semi-permanent pressure features are highly important for air mass advection (Papineau 2001; Hartmann and Wendler 2005a). During the winter, the meteorological features largely influencing the Interior of Alaska are the Aleutian low, the Beaufort high in the Canadian Arctic, and the Siberian high in Siberia, Russia (Overland et al., 1999; Rodionov et al., 2005; Shulski et al., 2010; Cassano et al. 2011). Additionally, the continental region of Alaska and northwest Canada are prone to the formation of high-pressure systems i.e., anticyclonic (AC) features (Bodurtha 1952, Bowling et al 1968; Curry 1983, 1987). The meteorology of the study region lies at the intersection of these features and their dynamical interactions. Moreover, the large-scale atmospheric systems covary in large-scale circulation patterns, such as with the Pacific Decadal Oscillation (PDO) (Mantua and Hare, 2002) and El Niño–

Southern Oscillation (ENSO), further modulating the regional weather dynamics and interannual climate variability (Hess et al, 2001). For instance, when the PDO phase changed to a primarily positive anomaly after ~1976, a warmer climate regime was brought into Alaska (Hartmann and Wendler, 2005a). Such an anomaly also intensified the Aleutian Low (Overland et al., 1999). Continental warmer conditions were also observed during the positive phase of the ENSO, modified by the PDO signal (Papineau, 2001; Hess et al., 2001; Hartmann and Wendler, 2005b; and more recently, Ballinger et al., 2023).

At the local scale, when anticyclonic (AC) conditions develop; characterized by the absence of solar radiation, extremely cold air temperatures, and snow- or ice-covered surfaces, a layered temperature inversion structure forms in the planetary boundary layer (PBL) (Mayfield and Fochesatto, 2013). This structure typically includes a Surface-Based Inversion (SBI) layer that forms near the ground, primarily driven by radiative cooling at the surface. Depending on the synoptic conditions, Elevated Inversion (EI) layers may also be present. These layered inversions significantly affect the PBL by controlling both the surface energy balance and turbulent fluxes (Mayfield and Fochesatto, 2013; Fochesatto et al., 2015). They also govern the dispersion of air pollutants emitted both at the surface and from elevated sources such as power plants (Mölders et al. 2011, 2012). The most prominent example of this structure; often referred to as a radiative boundary layer, occurs under synoptic AC conditions accompanied by a weak regional pressure gradient (Curry, 1983, 1987). In these cases, upper-level subsidence warms the atmospheric layers above the SBI due to adiabatic compression. This warming can create an EI without the need for Warm Air Advection (WAA) aloft (Mayfield and Fochesatto, 2013; Malingowski et al., 2014). Cassano et al. (2011) associated the coldest near-surface temperatures in Alaska's Interior with these synoptic AC conditions during winter. Beyond the synoptic scale, regional topography constrains atmospheric circulation under persistent AC conditions. This promotes small-scale inter-basin flows at the local and meso- β scales, further influencing surface turbulent fluxes and the energy balance. These dynamics lead to the development of Shallow Cold Flows (SCFs) (Fochesatto et al., 2015; Maillard et al., 2022; Mayfield and Fochesatto, 2019), which in turn modify the PBL structure and pollutant dispersion. When a strongly stratified SBI coexists with multiple EIs under stagnant regional AC conditions, vertical and horizontal mixing becomes extremely limited. This leads to the trapping of pollutants either near the surface or aloft between inversion layers within the PBL. Additionally, cold surface temperatures amplify emissions from local sources such as heating and traffic. This can result in severe air pollution episodes, including elevated concentrations of particulate matter (PM) (Cesler-Maloney et al., 2022). In some cases, these conditions are linked directly to the presence of a strong SBI (Cohen et al., 2007; Huff et al., 2010; Chen et al., 2011).

Fairbanks and North Pole are the two most populated cities in the Interior of Alaska where the wintertime air quality regularly exceeds regulatory thresholds under these very stable and cold large-scale conditions (with enhanced anthropogenic emissions; ADEC, 2019). Less populated Native Alaskan villages (e.g., villages in the Yukon Flats) are also seriously affected by the degradation of winter air quality (Edwin and Mölders, 2020) under similar conditions. Exacerbating this problem, regional pollution modeling is unable to accurately forecast air quality when the model fails to capture the depth and strength of the SBIs (Mölders and Kramm, 2010; Mölders et al, 2011, 2012) and radiative feedback linked to aloft EIs.

A better understanding of radiative and dynamic properties of the SBI and accurate modeling of the PBL processes are central to increasing our knowledge of the physics governing the wintertime Arctic PBL. Such advances are also critical for improving the simulation of local wintertime pollution and related processes (i.e. dispersion in stratified conditions, mixing, source apportionment, chemical processes, and wet and dry deposition). These important issues are goals of the ALPACA project (Simpson et al., 2024); the first comprehensive study coupling the PBL dynamics with air pollution chemistry in the Arctic wintertime. The results from ALPACA-2022 are relevant for sub- and pan-Arctic continental regions that also experience extreme meteorology with local anthropogenic emissions. ALPACA-2022 may also provide insight into the extent of which local Arctic pollution, when compared to remote sources, contributes to background Arctic haze (Thomas et al., 2019, AMAP, 2021).

3. Experimental Sites and Instrumental Platforms

The Interior of Alaska region, including Fairbanks and North Pole, is surrounded by two prominent orographic features: the Alaska Range to the south of Fairbanks and the Brooks Range to the north (Fig. 1a). The area in which ALPACA-2022 field experiment took place is situated in a basin, the Tanana Valley, with complex regional- and local-scale topography surrounded by the White Mountains to the north, Alaska Range to the south and Yukon-Tanana Uplands to the east (see Fig. 1b; Fochesatto et al., 2015). Connected to this main basin is a semi-enclosed valley to the north named the Goldstream Valley (Fig. 1c). The Goldstream Valley extends over approximately 10 km in the east–west direction and it is

sheltered by hills rising to 300–500 m on its southern border and to about 700 m height on the western side, near Ester Dome. Atmospheric flows affecting the area during winter are indicated in Fig. 2. Northerly, upper-level flows frequently descend from the White Mountains, while, to the west of Fairbanks, flows can be from the northwest due to a SCF channeled down the Goldstream Valley (Fochesatto et al., 2015; Maillard et al., 2022; Maillard et al., 2024) or from the northeast to southeast quadrant, carrying pollution with it from the main Fairbanks urban area. These features are important because the PBL structure and composition observed during ALPACA-2022 are influenced by the interaction of these features and the synoptic conditions and local-scale phenomena.

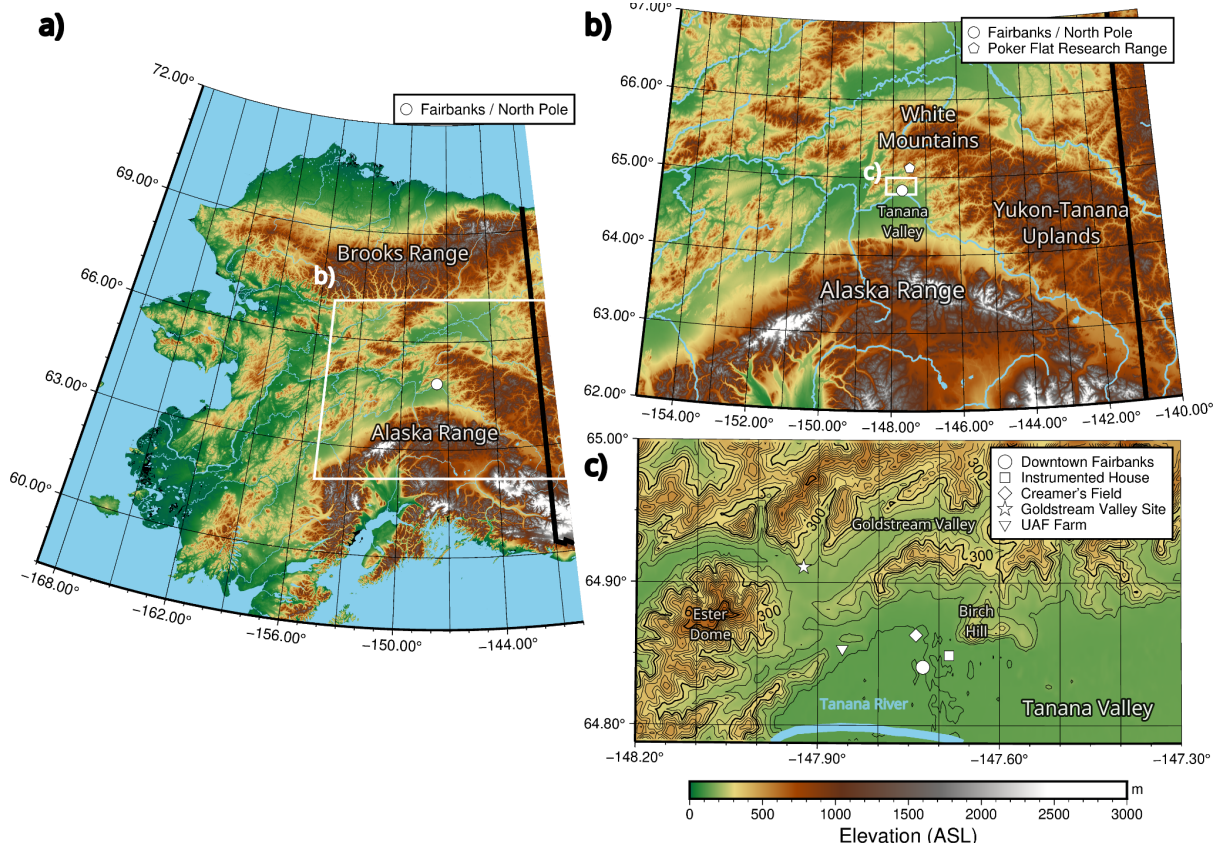


Figure 1. Geographic location of the ALPACA-2022 Field Experiment. a) Map showing Alaska with the outline for panel (b). The white dot indicates the Fairbanks area bounded to the south by the Alaska Range and to the north by the Brooks Range. Panel (b) shows the elevations and hills surrounding the Interior of Alaska region, with the White Mountains to the north, Alaska Range to the south, and the Yukon-Tanana Uplands to the east. The locations of Fairbanks and North Pole and the Poker Flat Research Range (PFRR) are displayed as well, with the area for panel (c) outlined. Panel (c) shows, in more detail, the experimental sites discussed in this paper: Downtown Fairbanks (with the Community Technical College (CTC), EPA NCore, and DOAS), Creamer's Field, the Instrumented House, Goldstream Valley, and UAF Farm. The color bar indicates the elevation in meters above sea level (ASL).

The main ALPACA-2022 experimental sites are indicated in Fig. 1c.

In particular, the University of Alaska Fairbanks (UAF) Farm was the site in the west of Fairbanks where comprehensive measurements were collected for the PBL dynamics and composition. Meteorological and surface radiative fluxes were also collected at the Creamer's Field and Goldstream Valley sites. The main site for aerosols and chemical composition was located at the Community Technical College (CTC) in downtown Fairbanks, near the Environmental Protection Agency (EPA) NCore monitoring site. Measurements at CTC and at the Instrumented House site, to investigate indoor and outdoor air pollution and remote sensing slant path DOAS observations, are described in detail by Simpson et al (2024). Here, we focus on the UAF Farm site observations and highlight some initial results from these observations.

Observations of the PBL composition and dynamics at the UAF-Farm site reflect the presence of surface urban air pollution sources, transport of these pollutants aloft with the influence of local meteorology, notably the intermittent presence of the north-westerly SCF originating from the Goldstream Valley.

Figure 2 illustrates the main atmospheric flows, emissions, and processes, together with the instrumentation and measurement strategy deployed at the UAF Farm site. To study the complexity of the PBL dynamics in the context of layered-air pollution processes, multiple instruments were deployed. This included taking surface samples (aerosol microphysics, trace gasses, snow depth, morphology, and chemical speciation), placing surface meteorological towers with radiative and turbulent fluxes (eddy covariance), and using a tethered balloon to measure vertical structure and composition (Helikite; thermodynamic, microphysical, aerosol, and trace gas measurements), a Doppler Lidar for wind direction and speed, and aerosol backscatter profiles, and a Microwave Radiometer (MWR) for temperature and relative humidity profiles.

ALPACA 2022 Field Study Boundary Layer Dynamics and Composition

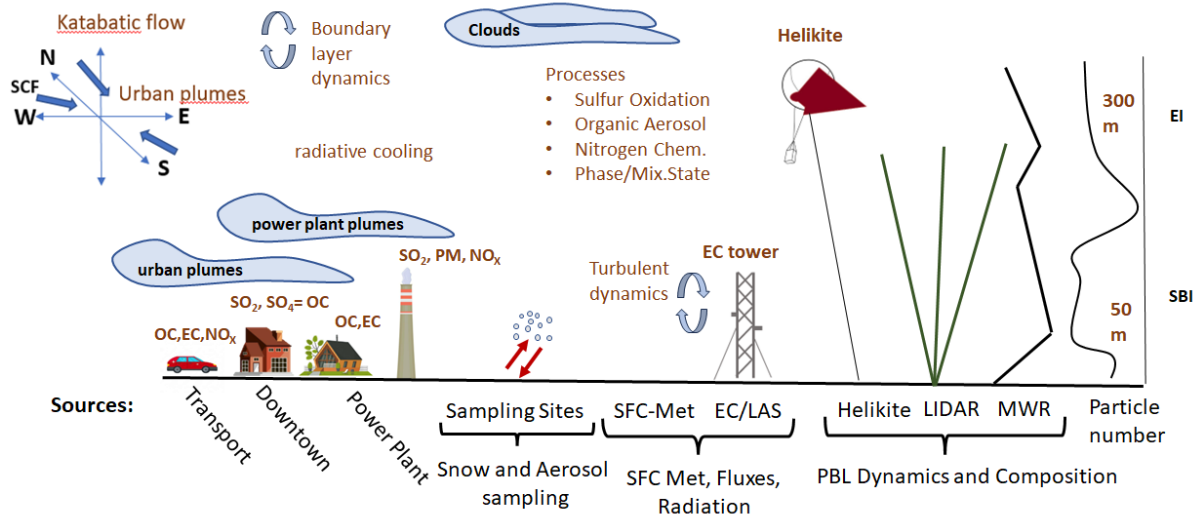


Figure 2. Schematic of the meteorological flows, emissions, and experimental setup during ALPACA-2022 at the UAF Farm site. Left: airflows over the UAF-Farm site (SCF: Shallow Cold Flow, urban plumes, and higher-level katabatic flows across the Tanana Valley), Center: factors influencing PBL composition near the surface (vehicle, residential, and commercial heating emissions), and aloft (power plant emissions). Right: Surface and profiling instrumentation.

Table 2 describes the instrumentation and research groups in charge of the different operations with the research hypothesis each instrumental platform addresses. In particular, goals G1-3 were addressed by co-locating instruments shown in Table 2 at the UAF Farm site, while goals G4-7 were addressed by co-locating instrumentation at the UAF Farm, CTC, Instrumented House, and DOAS sites in downtown Fairbanks and Trainor Gate Rd. (Simpson et al., 2024; see Fig. 1c).

Table 2. Meteorological and composition measurements during ALPACA-2022, with a focus on the UAF Farm site. See also Simpson et al. (2024). Research Goals refer to those listed in Table 1.

Instruments, Measurements, & Location	Instrument PI Institution	Research Goals
PBL Dynamics and Composition		

EPFL-Tethered balloon Helikite (Pohorsky et al., 2024) Payload includes RH, T, wind speed, ambient pressure, PM size and number via OPC, mini SEMS, and CPC, PM light absorption via STAP, offline sampling, CO ₂ , O ₃ , CO, BTEX (benzene, toluene, ethyl-benzene, xylene) analysis via online gas chromatography.	EPFL CNR-ISAC	G4-5-6
MicroMegas balloon trace gas payload: O ₃ , CO, NO, NO ₂ (Barret et al., 2024) UAF Farm	CNRS-LAERO	
Microwave Radiometer PBL T and RH profiles at 2 min time resolution UAF Farm	UAF, LMD-IPSL	G1, G2, G3
Doppler Lidar Wind speed and direction and aerosol backscattering profiles at 10 min resolution CTC and UAF Farm (see Fig. 3)	UCLO-OPAL CNRS-LATMOS	G1, G3, G4
Surface Met, Fluxes, Radiation and Composition (Farm) Observations		
3 m-Eddy-Covariance Tower Surface radiative (SW and LW) turbulent fluxes (u, v, w, T, H ₂ O and CO ₂ ; 10 Hz) UAF Farm	UAF, LMD-IPSL, UVic.	G1, G2, G3
10 m eddy covariance tower Coupled to a CPC and OPC at 1 Hz UAF Farm	CNR-ISAC	G1, G2, G3, G6
2 m met. station wind direction and speed, RH, T, SW and LW radiation fluxes UAF Farm	EPFL	G1, G2, G4
10 m met. tower: SW and LW radiative fluxes, T, and wind speed and direction VOCs and aerosol composition UAF Farm	CNR-LATMOS UAF EPFL UAF LCE, CNR-ISAC	G1-2-3
Snow Sampling		
Nitrate multi-isotopic analysis ($\delta^{15}\text{N}$, $\delta^{17}\text{O}$, $\delta^{18}\text{O}$) and aerosol composition UAF Farm, NCORE, Poker Flat Research Range	CNRS-IGE CNRS-LATMOS	G6
Ionic composition, metals, and organic tracers, at UAF Farm	CNR-ISAC*	G6

*RH: Relative Humidity probe, T: Air Temperature, PM: Particulate Matter, OPC: Optical Particle Counter, mini-SEMS: Scanning Electrical Mobility Sizer, CPC: Condensation Particle Counter, SW: Shortwave Radiation, LW: Long Wave Radiation. *Coordinated by CNR-ISAC and carried out in collaboration with the University of Venice.*

The extremely harsh winter environment made continuous operations very challenging. This meant that certain measurements had periods of interruption, and it was not possible to make daily flights with the Helikite (limited also by flight restrictions). Twenty-four flights were made, for the first time in a polluted Arctic wintertime environment. Figure

3 shows the timeline of instrument operations and identifies periods where measurements of the PBL dynamics and composition were collected simultaneously during the experiment.

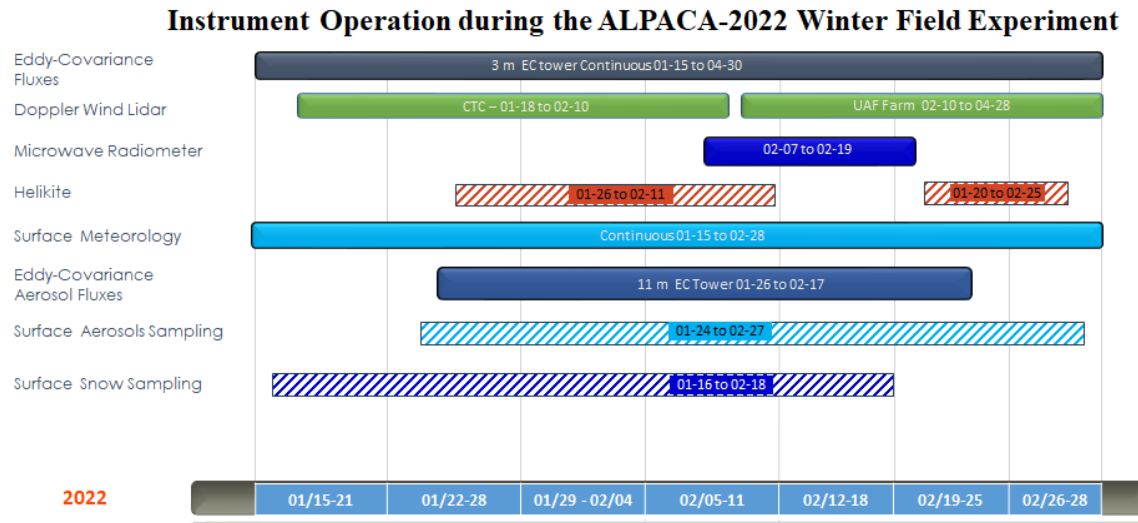


Figure 3. Time diagram of the instruments and platforms operated during ALPACA-2022: from 17 January to 28 February, predominantly at the UAF Farm site. Hatched areas indicate discontinuous operations.

4. Meteorology: synoptic and local framework

An examination of temperature records during the ALPACA-2022 field experiment and climatological maximums and minimums for the area shows warmer minimum temperatures throughout the experiment. However, the maximum temperatures were colder than the climatological mean. This is consistent with more variable synoptic conditions and AC conditions with shorter life cycles (see Section 2).

Local thermodynamic radiosonde information is shown in Fig. 4 from the Fairbanks International Airport for the entire campaign from 0:00 UTC 01-15-2022 to 0:00 UTC 03-01-2022. Figure 4 shows the isentropic levels (equivalent potential temperature contours) superimposed with the relative humidity field. The color bar on top indicates the presence of anticyclonic systems (red; AC), cyclonic conditions (blue; C), and transient synoptic conditions (purple; T). Indicated by the figure, the expansion of the isentropic contours show the stabilization of the lower layers when AC systems form in the area (AC1, AC2, and AC3).

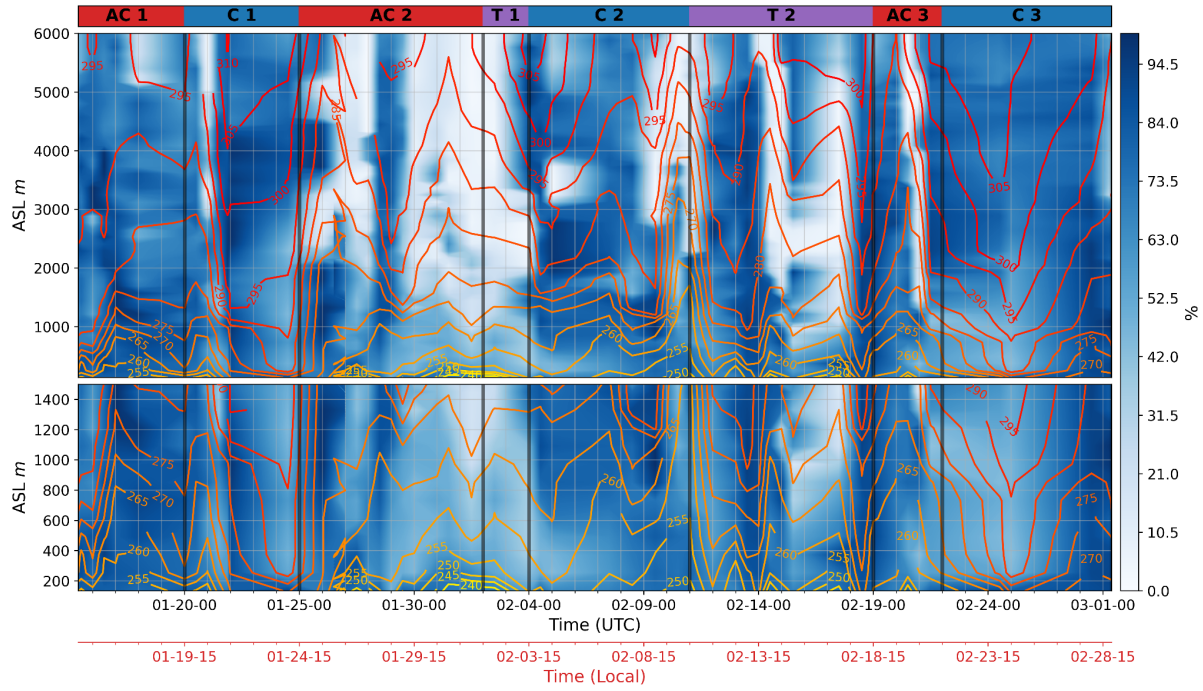


Figure 4. Upper and lower tropospheric equivalent potential temperature (solid contour lines at 5 K intervals) with superimposed relative humidity on a white-blue color scale. The gridding was derived from successive radiosonde-based thermodynamic profiles collected at the Fairbanks International Airport every 12 hrs between 0:00 UTC 15-01-2022 and 0:00 UTC 03-01-2022. Anticyclonic conditions are marked by AC in the top bar (red), with cyclonic conditions marked by C (blue), and transitioning conditions marked by T (purple).

Large-scale synoptic meteorological conditions for three synoptic cases during the experiment (AC2, T2, and C3) are shown in Fig. 5, based on the ECMWF ERA5 high resolution reanalysis datasets (surface mean sea level pressure (MSLP) (top panels) and geopotential height at 500 hPa (Z) (bottom panels)).

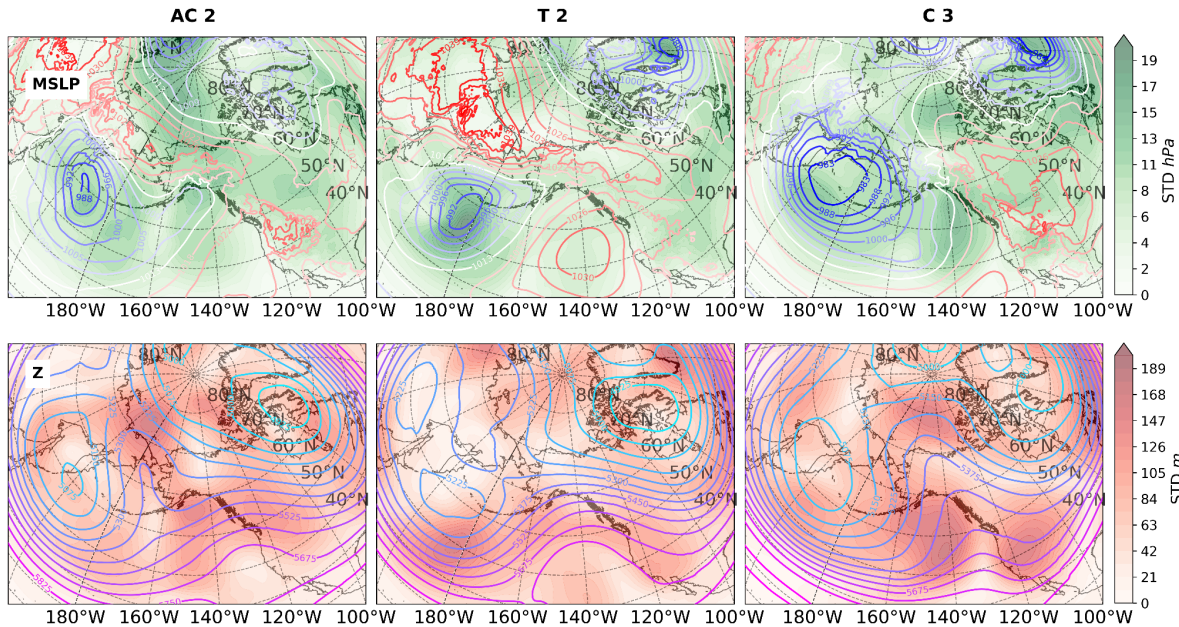


Figure 5. Averaged ECMWF ERA5 Mean Sea Level Pressure (MSLP), top panels, and geopotential height at 500 hPa (Z), bottom panels, of the selected synoptic periods: AC2, T2, and C3 (denoted in Fig. 4). The shading corresponds to the standard deviation of the respective variable.

In terms of the synoptic conditions, AC2 is an important period to note, with anticyclonic conditions over the Interior of Alaska building when high pressure systems over Siberia and mainland Canada connect, blocking the Aleutian low to the south and extending its duration over central Alaska, strengthening from Jan 31 to Feb 1. This is illustrated by the dry air masses aloft and in the PBL, as seen in Fig. 4. AC2 is followed by a transition period (T1) from Feb. 2 to Feb. 4, when a **low-pressure** system moves northeastward from the Aleutians, establishing a north-south, high-low pressure gradient over Fairbanks. After Feb. 4, a series of secondary lows form off the main Aleutian low pressure area and move northward, maintaining constant cyclonic conditions over Fairbanks until Feb. 11 (C2). After the last low pressure moves eastward over Canada, the persistent Siberian high pressure intermittently extends and connects with a **high-pressure** system over the Gulf of Alaska from Feb. 11 to Feb. 19 and is periodically interrupted by low pressure systems arriving from the Bering Sea (transition period T2). After T2, there is a brief anticyclonic period, AC3, due to high pressure from the Arctic Ocean, north of the Chukchi Sea, moving over the Interior of Alaska. On Feb. 22 it is displaced by the northerly extension of the Aleutian low which dominates the synoptic situation for the remainder of the field campaign (C3; cases beside AC2, T2, and C3 are not shown).

5. Evolution of representative variables during ALPACA-2022

In this section, a set of surface and vertical observations describing the PBL dynamics and composition during the central part of the ALPACA field intensive campaign are presented. The observations were conducted in the UAF Farm site and are shown in Fig 6. The observations illustrate their variability in relation to the large-scale synoptic forcing and PBL dynamics. Fig. 6a shows ERA-5 specific humidity values at air mass origins labeled 5 days before arrival in a vertical profile over the UAF Farm site, calculated from the Reading Offline Trajectory (ROTRAJ) Lagrangian transport model (Methven et al., 2003). Gradients in this field highlight large-scale shifts in influences on the vertical profile of air mass over the UAF Farm site. Variations in in-situ specific humidity (q), and other meteorological variables (Figs. 6b,c,f) also respond to the evolving synoptic situation. For example, the buildup of AC conditions results in strong surface radiative cooling (net radiation (R_{net}) < 0 ; Fig. 6f) with a reduction in q ($q < 0.004 \text{ kg/kg}$). Conversely, under cyclonic (C) and transient (T) synoptic conditions, relatively moist air masses with elevated q (Fig. 6b) are indicated aloft as a result of WAA from the south. In terms of the PBL state, the buildup of SBIs can be diagnosed from the following cooling periods, based on the simultaneous decrease in temperature at levels near the surface: Jan. 27-28, Jan. 29-Feb. 1, Feb. 3-4, 8, 11, 16, and 17. As noted before, such periods start due to the high pressure over the region stagnating the flow, suppressing cloudiness, and, therefore, intensifying the surface radiative cooling ($R_{net} < 0$; Fig. 6f). The MWR observations were only available for a limited period during the campaign but provided important insights into the temperature evolution in the PBL, as shown in Fig. 6c (and aloft; not shown).

At the local scale, the surface cools down faster than the atmosphere, deepening the cooling effect in the PBL, as indicated by the negative ambient temperature gradient at different heights (Fig. 6c). SBIs form when the cooling rate is observed to increase across the atmospheric layers with maximum rates in the near-surface levels. As described in Section 4, the AC systems observed during ALPACA-2022 were interrupted by the intrusion of cyclonic systems or increasing shortwave downward radiation (due the transition out of the Arctic winter) resulting in the PBL column warming at levels above the surface, breaking up the SBIs. As a result, the surface layer state evolves from stably stratified conditions to be nearly

adiabatic, resulting in a mixing layer at the end of the episode (SBI break up), erasing the near surface stratification (see Figs. 6c,f.).

During periods where an SBI builds up (e.g. Jan. 28, 31, and Feb. 1), the Doppler backscatter Lidar provides an indication of the aerosol content above 40 m, showing the presence of plumes aloft in the stratified environment (Fig. 6d). However, these periods are governed by an AC, with near surface winds at less than 4 m/s, enabling local sub-mesoscale flows to occur. This is noted in Fig. 6e, where wind speeds increase, dispersing the aerosol loading at the CTC site during the periods of Jan. 27-28 and Jan. 30-31. This is an important consideration, since local flows could disrupt the SBI and mixing and dispersing aerosols (Maillard et al. 2022). Conversely, when stable conditions are not interrupted, surface air pollution can accumulate, as illustrated in Fig. 6g with the time series of carbon monoxide at the UAF Farm site. During the experiment, CO concentrations increased from ~100 ppb to 500 ppb or higher during stable AC conditions with strong SBIs.

Following the synoptic conditions (Fig. 4), the time series of snow depth rises during the warming periods (i.e., transients and cyclonic conditions), occasionally providing precipitation after Feb. 4. To examine the chemical signatures on the snow surface, the time series of Pb and Na are represented Fig. 6i. Two main periods can be distinguished; dry deposition from Jan. 23 to Feb. 2, followed by a period with interspersed wet deposition pronounced after Feb. 4. In this case, the Pb (as a representative for elements from anthropogenic combustion sources) in snow samples increases during the long AC2 period, where large-scale subsidence rises (negative vertical velocity), favoring dry deposition. Under such conditions, pollution from plume stacks, capped by a multilayered PBL (Mayfield and Fochesatto, 2013) limits the dispersion of pollution under extreme cold conditions triggering ice crystals formation and sedimentation/deposition (Ohtake and Huffman, 1969) and more recently (Hartl et al 2023). On the other hand, the Na time series concentration is observed to rise when the meteorological conditions change at the end of the AC2 episode and through T1 and C2 as result of wet deposition and exchange of air masses.

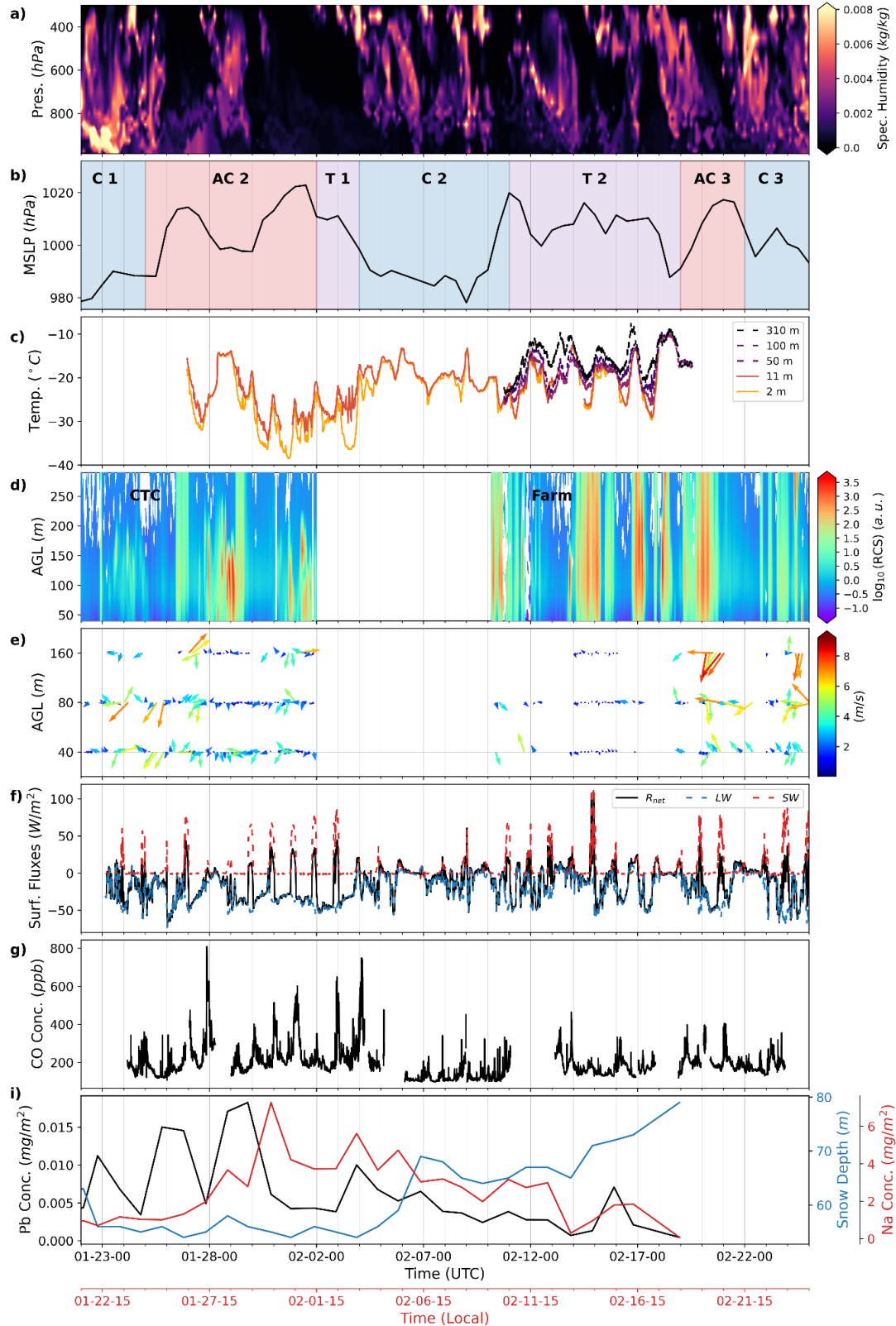


Figure 6. Multiple time series representing the period Jan. 23 to Feb. 25, including PBL dynamics and composition. (a) specific humidity values at 5-day back trajectory origins arriving in a profile of arrival altitudes above the UAF Farm site, (b) is a composite plot illustrating the sea level pressure at the UAF Farm site and identified synoptic features dominating the atmospheric flow over central Alaska (from Fig. 4). (c) shows the ambient

temperature retrieved from the 10 m met. tower at 2 and 11 meters and from the MWR vertical profiler at 50, 100 and 310 meters above ground level (AGL). (d) and (e) are, respectively, the apparent backscattering at 1550 nm laser wavelength and the wind speed and direction at 40, 80 and 160 m AGL derived from Doppler Lidar observations. (f) is the time series of longwave (LW) and shortwave (SW) radiation and the resulting net radiation (R_{net}) flux. (g) is the time series of carbon monoxide concentration. (i) is the time series of chemical composition including Pb and Na concentrations of the snow surface, with the snow depth (cm).

Overall, the results from the ALPACA-2022 field experiment show strong synergy between different measurements, enabling a comprehensive description of the main drivers influencing the PBL and air pollution during the Arctic wintertime.

6. Results on PBL dynamics

In this section we highlight some of the important aspects of the PBL dynamics that are critical ingredients in advancing our understanding of the high latitude, winter air pollution. As noted earlier, longwave (LW) radiative forcing plays a fundamental role in controlling the PBL state in the cold and dark atmospheres and is linked to the synoptic-scale variability. Radiative forcing has two main effects on the PBL state: surface radiative cooling driving the buildup of the SBI and increasing LW-down, warming the surface and initiating the breakup of the SBI. To illustrate the SBI build up and break up, we highlight the period from 12:00 UTC Feb. 15 to 22:00 UTC Feb. 16. The temperature evolution at different heights, the surface radiation terms, and the winds are shown in Fig. 7. This period was dominated by radiative conditions where the SW radiation, sensible heat flux (H), and turbulent kinetic energy (TKE) were all absent and occurred during a transient condition (T2, see Fig. 4 and 8). At this time, the polar front was oscillating over the Fairbanks region (not shown), leading to clear skies when situated to the south, and increasing cloudiness when it was situated to the north. As shown in Fig. 7, the period starts with surface radiative cooling followed by radiative warming initiated from the upper atmospheric levels. It is important to distinguish here that direct LW-down radiative forcing is a top-down radiative forcing. The temperature at several altitudes in the PBL is shown in Fig. 8a from the MWR data. These heights were selected to provide a detailed description of the thermodynamic response of the PBL and of the lower free troposphere. As the large-scale sea level pressure builds up (see Fig. 6b) the air mass close to the surface experiences an overall cooling but doesn't aloft (above 800 m). From 0 to 250 m, the PBL experiences a columnar cooling over the first 4

hrs. driven by the surface radiation deficit $R_{net} < 0$ caused by $LW < 0$ (Fig. 7b). Then, after Feb 16, 2:00 UTC, the formation of the SBI leads to an acceleration of the radiative cooling in the layers near the surface in the following 4 hrs. After this rapid cooling period, the cooling rate slows down while LW_{net} and R_{net} remain negative. For the whole event, the surface radiative cooling is sustained for about 14 hrs with R_{net} ranging from -40 to -20 W/m².

However, around Feb. 16 at 12:00 UTC, the upper levels (>250 m) start warming slightly and, by downward radiative transfer, LW changes from negative to zero or slightly positive by the end of the period. This indicates that LW-down is larger than LW-up (i.e., “warming from above”) and as a result the PBL air mass and the surface warm up, since shortwave (SW) is negligible. In terms of surface winds, the UAF Farm site experienced wind directions alternating between north-northwest to south-southeast after Feb. 16 at 2:00 UTC, with wind speeds less than 2.5 m/s. This indicates that changes in the wind directions and momentum imbalances cannot be the driver of the SBI break up. Therefore, these results show a case of how the PBL state responds to the synoptic meteorology. Evaluation of the number of SBI build and break up cases, combined with analysis of air pollution levels, will provide insights into processes influencing air pollution accumulation and dispersion.

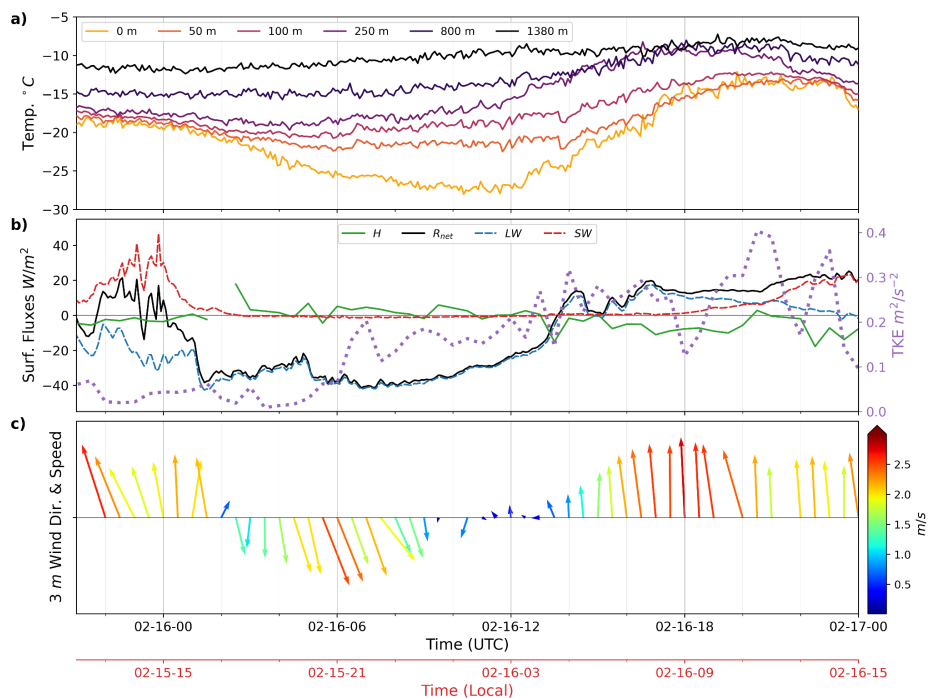


Figure 7. PBL dynamics case study representing the period Feb. 16 to Feb. 17, 2022. (a) shows the ambient temperature time series retrieved from the MWR vertical profiler at 0, 50, 100, 250, 800, and 1380 m AGL. (b) is the time series of LW, SW, and resulting R_{net} fluxes.

Superimposed is the computed sensible heat flux (H) and turbulent kinetic energy (TKE). (c) shows the time series of surface wind speed and direction through wind barbs.

7. Results on PBL composition and Air Pollution Study

7.1 Occurrence of Shallow Cold Flows and Connecting ALPACA sites

The extent to which shallow cold flows (SCFs) influence the thermodynamic structure of the PBL, including SBIs, and thus pollution levels, in the Fairbanks area is an open research question. An SCF originates from the Goldstream Valley, as noted earlier, but the extent to which this flow extends over the main urban area has not been documented. Here, an example is presented where this flow was observed at the downtown CTC site by the wind lidar (above 40 m from the ground) and data collected on the CTC building (23 m) on Jan. 23, occurring during a cyclonic weather condition (C1). Figure 8 represents the combination of surface meteorological and chemical composition time series and vertical profiling of wind speed and direction, as well as aerosols mass transport seen by the lidar backscattering.

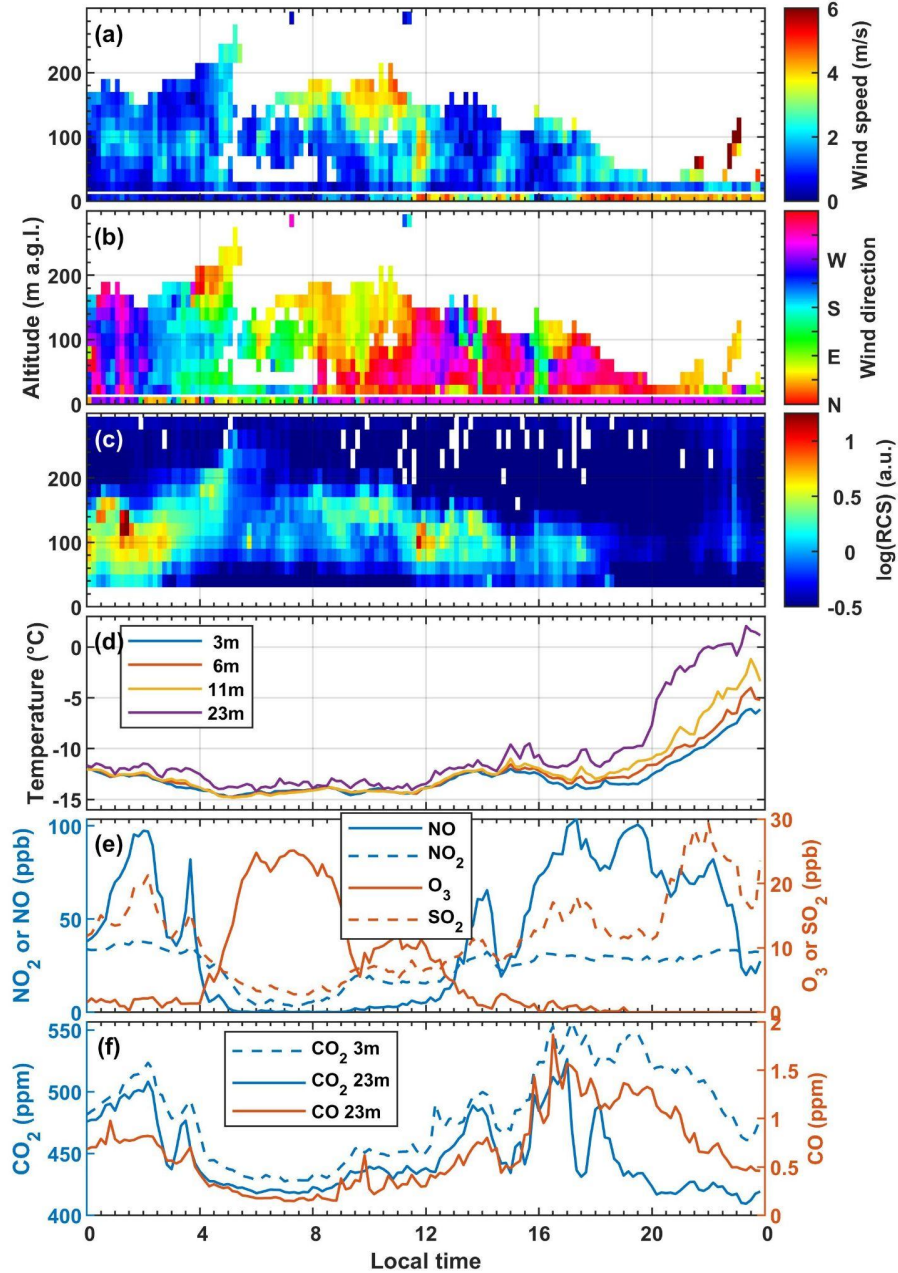


Figure 8. Doppler wind lidar observations, temperature, and trace gas concentrations at the CTC site on Jan. 23, 2022: (a) wind speeds, (b) wind direction, (c) lidar Range-Corrected Signal (RCS), (d) temperatures at different altitudes, (e) NO₂, NO, O₃ and SO₂ concentrations, and (f) CO₂ and CO concentrations.

Wind speeds and directions measured at the CTC building (23 m above ground; data shown above the white line), and at the UAF Farm site (11 m above ground; data shown below the white line), fall within the lidar blind zone shown at the bottom of Fig. 8 panels (a) and (b). The Shallow Cold Flow (SCF) was first observed near the surface at the UAF Farm around 08:00 LT (AKST), with prevailing northwesterly winds. This flow persisted at the UAF Farm site until approximately 20:00 LT (Fig. 8b). The SCF reached the CTC site around the same

time (08:00 LT), where it was detected by the wind lidar above 40 m. Horizontal wind speeds at this altitude reached 4–5 m/s, with wind directions shifting to north-northwesterly. The flow extended vertically up to about 140 m and persisted until between 18:00 and 20:00 LT, depending on altitude. Vertical wind speeds during this event were generally light and predominantly positive, remaining below +0.2 m/s (data not shown). Wind speeds of up to 2 m/s were also observed on the rooftop of the CTC building just before 12:00 LT and again around 14:00 LT, in agreement with the lidar data. These observations suggest that the SCF may have induced mechanical shear in the atmosphere above the surface. Such behavior has previously been documented at the UAF Farm, where SCFs led to mechanical shearing that weakened strongly stable boundary layer conditions and resulted in weak surface stability (Fochesatto et al., 2015; Maillard et al., 2022). However, similar effects have not been observed over downtown Fairbanks. The potential influence of the SCF on surface-level pollutant concentrations at both the UAF Farm and the CTC site is also considered here. Before the SCF's arrival, winds came from the east, and surface pollution levels were low. This was likely due to the absence of a strong temperature inversion below 23 m. At the same time, nitrogen oxide (NO) concentrations were also low, reducing ozone (O_3) destruction. This, combined with the possible mixing of cleaner background air masses, resulted in elevated O_3 concentrations. After the SCF arrived, concentrations of pollutants such as sulfur dioxide (SO_2), nitrogen dioxide (NO_2), and carbon dioxide (CO_2) increased at the surface. Elevated levels of carbon monoxide (CO) and CO_2 were also recorded on the roof of the CTC building. Concurrently, the lidar's relative backscatter signal (RCS) showed the presence of aerosol plumes aloft during periods of north-northwesterly flow. Finally, weak surface stability, evident in the small vertical temperature gradient, appeared to persist throughout the SCF event. This could be attributed to the increased mechanical shearing aloft associated with the SCF.

This may have led to the downward transport of elevated sources of pollution, notably from power plant stacks, observed in the lidar RCS above 40 m. A case of potential downward mixing appears to coincide with higher winds at 14:00 LT and increased surface NO, NO_2 , SO_2 and surface/CTC roof CO_2 concentrations. The lack of a strong surface SBI may also have induced upward mixing of surface air pollution, e.g. from vehicles or residential/commercial emissions, space heating, or the transport of surface air pollution to the CTC site from the north.

After 16:00 LT, the SCF appears to be eroded from aloft, with light winds and oscillating wind directions at 23 m. As the winds decreased, the lowest levels became strongly stable with increasing SBI strength and pollutant concentrations (notably surface NO and CO_2) increased significantly. CO_2 and SO_2 also increased at 23 m. The SBI became much more marked after 19:00 LT, and only surface SO_2 remained high, likely due to the residential (oil) heating emissions in the evening. CO_2 also remained elevated at the surface but decreased to background levels on the CTC roof. This is due to the arrival of a cleaner air mass aloft. By

this time, the SCF had been eroded, with increasing wind speed and easterly flow. Collection of wind lidar data was hampered by the lack of particle backscatter but a few signals with high wind speeds (5-6 m/s) from the east were detected. To illustrate the potential connection between ALPACA sites the air mass motion in the PBL is shown in Fig. 9 by means of wind roses at the CTC and UAF Farms sites using near-surface and Doppler lidar observations and results from the EPA-WRF (Weather Research and Forecast) model, which was run including the assimilation of surface, radiosonde, and lidar data (see Brett et al., 2024 for details). It shows that the urban downtown area of Fairbanks was generally influenced by light, north to northeast winds but also by moist air masses from the south and southeast during transient and cyclonic conditions. The UAF Farm site was influenced by the northwesterly SCF up to an altitude of around 50 m. The EPA-WRF model generally captured the wind speeds and directions at CTC but, despite assimilation of lidar winds during February, had difficulties simulating the SCF above the surface (40 m). This may be due to model resolution (1.33 km) or lack of adequate PBL-surface feedback, influencing the modeled surface energy budget (Maillard et al., 2024).

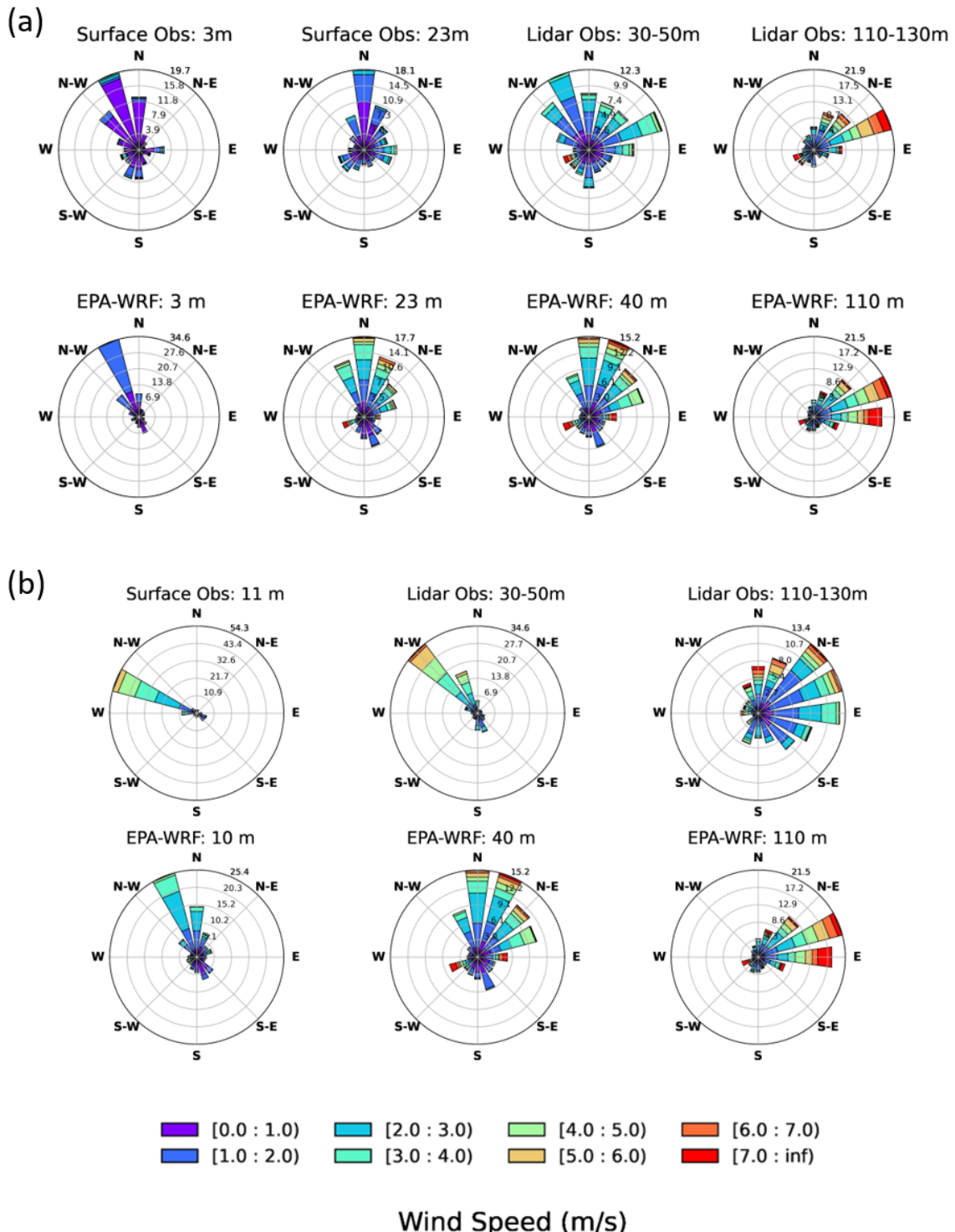


Figure 9. Average wind roses using observations (top rows) and EPA-WRF results (bottom rows) at CTC (Jan. 17 to Feb. 8) (a) and the UAF Farm (Feb. 8 - 25) (b). Top-left panels are near-surface observations at 3 m and 23 m (a) or 11 m (b), top-right panels are the averaged 30-50 m and 110-130 m winds retrieved by the Doppler Lidar. Bottom panels are EPA-WRF model winds (averaged 1 hr output) for the same periods as the observations.

Despite the modeling and experimental datasets shows some indications of such correspondence in the PBL airmasses, a more in-depth analysis is required to further investigate the extension of the SCF into downtown Fairbanks, especially since it may have led to the vertical exchange of pollutants. As Fig. 8 describes the SCF was eroded by the changing wind regime aloft, strongly stable conditions returned, trapping the pollution below the SBI. Similarly, Fig. 9 describe a statistical behavior of the wind profiles combining experimental and model results potentially suggesting a common airmass over both experimental sites.

7.2. Influence of synoptic-scale dynamics on urban pollution ventilation. Case study of January 27-28, 2022.

On Jan. 27 and 28, 2022, a shift to cyclonic synoptic conditions i.e. WAA, occurred, leading to an erosion of the SBI (Mayfield and Fochesatto 2013) and a dilution of near-surface pollution with cleaner air from aloft. During such a synoptic transition, the accumulated polluted air mass can be transported locally from downtown to the UAF Farm site, thereby affecting pollution levels in suburban areas. This dynamical exchange shows how strong synoptic forcing leads to pollution dilution and transport over the entire Fairbanks area.

On Jan. 27, at 3:30 LT, the surface stratification started weakening in response to increased cloud cover (Fig. 10a) due to the large-scale cyclonic system. At the same time, Rnet increased from -55 W/m^2 to -15 W/m^2 between Jan. 26 at 15:30 LT and Jan. 27 at 8:00 LT (not shown here). Therefore, in the absence of strong radiative cooling, there was a notable decline in the strength of the westerly flow, coinciding with a shift in prevailing surface wind direction from north westerly to easterly (Fig. 10b). Under a weaker SBI, with easterly wind influence, surface pollution was slowly advected from downtown Fairbanks to the UAF Farm. Fig 10b shows how the particle number concentration at UAF increased, reaching levels comparable to those observed downtown after 12:00 LT. Until 20:00 LT, the wind speed observed by the lidar at the CTC was fairly low ($< 2 \text{ m/s}$) and no dominant wind direction could be defined. The backscatter signal was also weak above ~ 150 to 200 m , indicative of an EI. The RCS

signal indicated plumes aloft trapped by the EI, likely originating from the Aurora power plant (Brett et al. 2024; see Fig. 11c).

After 20:00 LT, the lidar showed increased wind speeds above 200 m, with a northerly direction. Figure 11 shows how the WAA from the north eroded the surface cold air layer, descending toward the surface, finally reaching the surface shortly after midnight (LT). During that time, the lidar also showed light snowfall between 20:00 LT from Jan. 27 to 5:00 LT Jan. 28. A Helikite flight was performed between 23:00 LT on Jan. 27 and at 0:20 LT, Jan. 28 (see Fig. 12). The Helikite altitude is shown by the dotted line on Fig. 11 and Figure 12 shows the collected measurements. The colors of the dots represent the chronological evolution of the flight. During the first ascent, a polluted surface layer with increased particle concentration and fully depleted O₃ was observed up to 25 m (Fig 12b,c). Above 25 m, the concentration decreased and reached background values ~80 m. For each profile, the temperature measurements show that the warm air mass aloft descended and reached the surface on the last profile, resulting in a complete dilution of all pollutants. The particle concentration measured at the surface dropped drastically at the end of the Helikite flight (indicated by the gray shading in Fig. 10c) but surface concentrations at the CTC site only dropped 3 hours later. This lag could be explained by the effect of the urban canopy, which slowed down the downward erosion by the warm air aloft. This case study demonstrates the manner in which synoptic forcing initially influences local dynamics via the surface radiation balance, resulting in a broader horizontal spread of Fairbanks's pollution at the ground level and, ultimately, is replaced with a warmer and cleaner air mass.

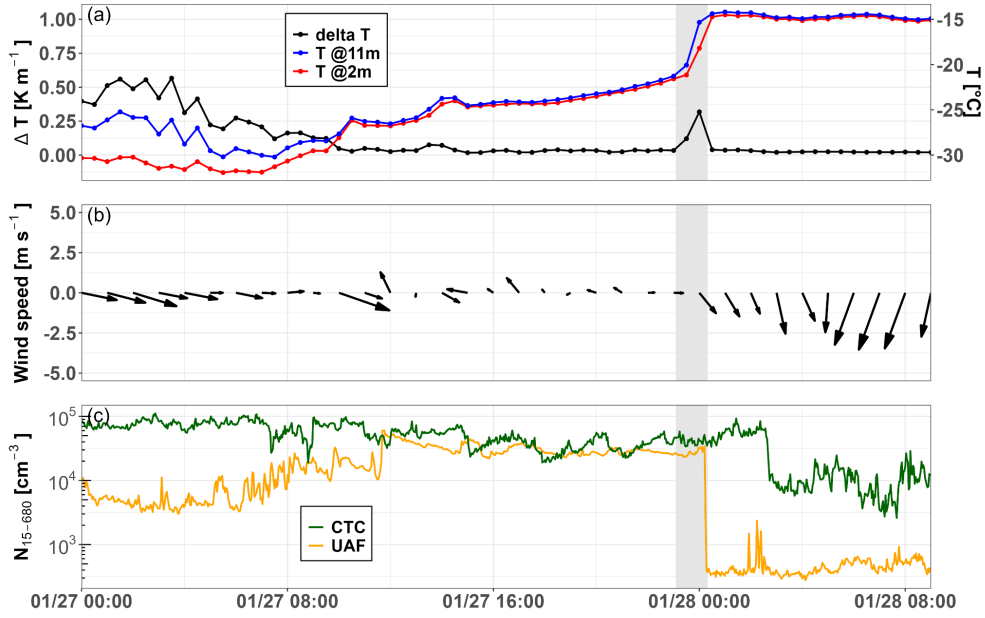


Figure 10: Time series (in local time) of (a) temperature at 11 and 2 m above ground (blue and red) and temperature difference, (b) wind vectors at the UAF Farm. (c) shows the particle number concentration from 15 to 680 nm at the UAF Farm (orange) and CTC (green). Grey shading indicates the period of vertical measurements with the Helikite.

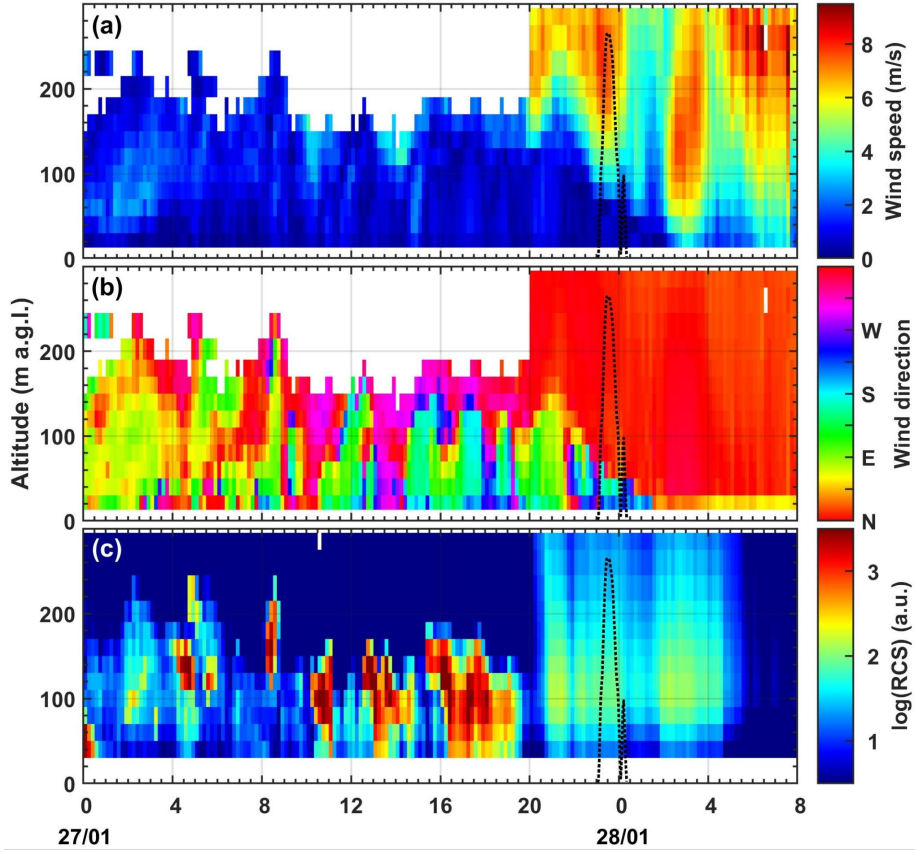


Figure 11: (a) Wind speed, (b) wind direction, and (c) particle backscattering from the doppler wind lidar (in local time). The dashed lines represent the Helikite's altitude during its flight. Wind observations from the weather station atop the CTC building (23 m above ground) were included in the lidar blind zone on panels (a) and (b).

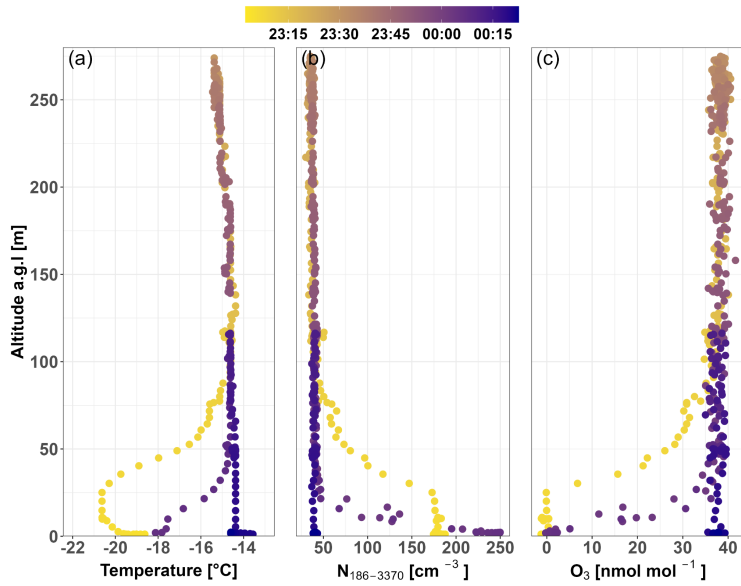


Figure 12: Vertical profiles from Helikite in situ measurements of (a) temperature ($^{\circ}\text{C}$), (b) particle number concentration from 186 to 3370 nm (cm^{-3}) and (c) O_3 (nmol/mol). The Helikite altitude is shown by the dotted line on Fig. 11. The colors of the dots represent the chronological evolution of the flight.

7.3 Power plant plume transport in the wintertime PBL

Vertical profiles collected by the Helikite at the UAF Farm showed elevated concentrations of NOx between 100 to 150 m (AGL) toward the end of a flight that took place between 22:00 LT on Feb. 3 and 3:00 LT on Feb. 4 (see Fig. 13). NOx concentrations of up to 75 ppb were observed, which are well above background levels. The high NOx in the plumes induced complete titration of O_3 to near zero due to the destruction of O_3 by NO and the lack of sunlight to photolyse NO_2 (and reform O_3) during this nighttime flight.

The flight took place during the transition (T1) from a cold, stable anticyclonic condition (AC2) to warmer, weakly stable cyclonic conditions (C2). This led to changes in wind direction (derived using the balloon position, see Fig. 14.) from northeasterly to easterly at altitudes where the plumes were observed around 2:00 to 3:00 LT on Feb. 4. The wind lidar was located at CTC during this flight. Interestingly, aerosol pollution was detected at similar times in the lidar RCS between 100-150 m and lidar wind directions show good agreement with the wind directions derived from the balloon position above 80 m. In contrast, the balloon wind directions show that a northwesterly SCF was present at the UAF Farm below 80 m which was not observed by the lidar at CTC. Measured trace gasses and aerosols (latter

not shown) were enhanced above background levels below 80 m. This may be due to transport of emissions from the Goldstream valley to the measurement location by the SCF.

To investigate the origin of these plumes, emission tracers were simulated using the FLEXPART-WRF particle dispersion model, including surface and power plant emissions. The emissions from power plant stacks in the Fairbanks region varied temporally, and took into account plume injection and PBL stability, such as the presence of EIs or SBIs (see Brett et al., 2024, for details). Figure 15 shows the spatial distribution of total power plant tracers (given as arbitrary units) before the Helikite flight at 18:00 LT on Feb. 3 (panel a), at 2:00 LT on Feb. 4 (panel b), and at 7:00 LT on Feb. 4, averaged over 100-150 m.

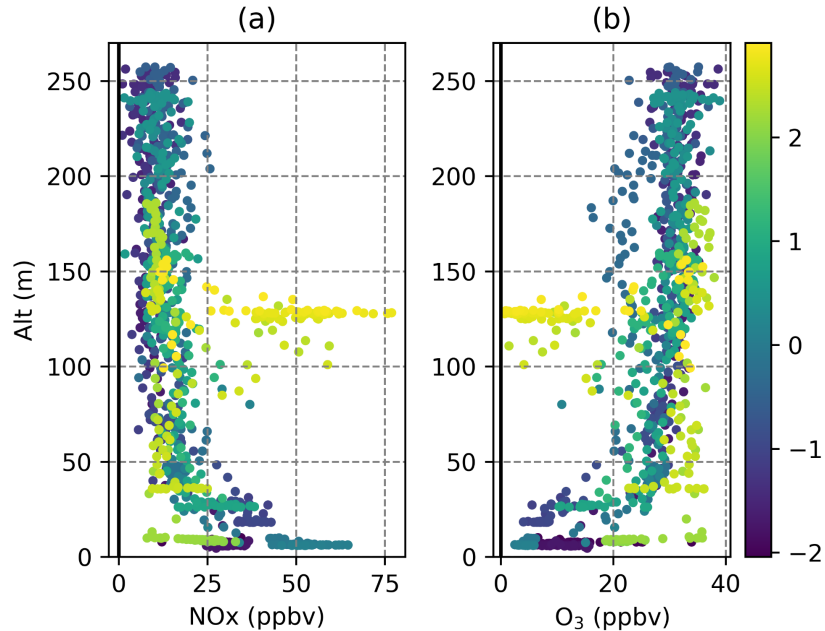


Figure 13. Vertical profiles from the Helikite flight from 22:00 LT on Feb. 3 to 3:00 LT on Feb. 4 showing (a) NO_x (b) O₃ measured using the MICROMEGAS instrument, coloured as a function of time during the flight (black to yellow with zero being 0:00 LT on Feb. 4).

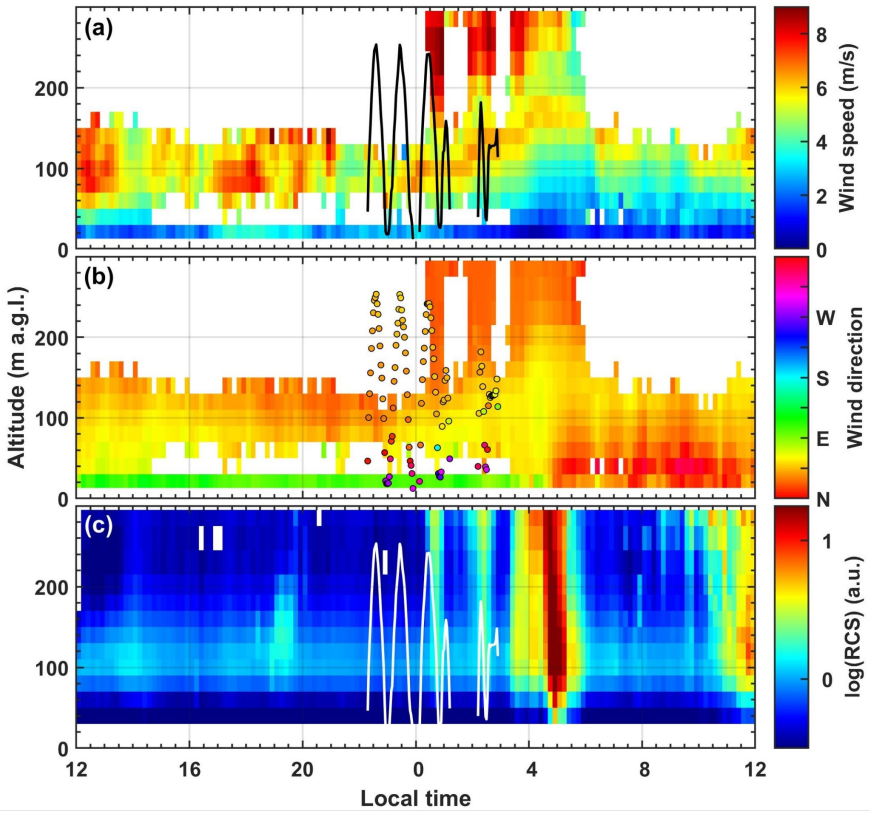


Figure 14. Time series of (a) wind speed, (b) wind direction and (c) particle backscattering from the wind lidar at the CTC site. The time and altitude of the Helikite flight at the UAF Farm site are shown in panels (a) and (c). On panel (b), the colored dots represent the wind direction derived from the balloon position. Wind observations from the weather station atop the CTC building (23 m above ground) were included in the lidar blind zone on panels (a) and (b).

A plume is simulated passing over the UAF Farm at the same time as the Helikite flight. Following the analysis discussed in Brett et al. (2024), the plumes originated from the Doyon power plant, located in eastern Fairbanks. Other stacks do not appear to contribute to the observed plumes. However, the simulated plume is transported to the south of the UAF Farm during the Helikite flight (Fig. 15b). Before and after the Helikite flight, the plume is simulated closer to the UAF Farm (panels a and b). As explored in Brett et al. (2024), the modeled EPA-WRF winds used to drive the model were from the northeast, rather than from the east in the observations, leading to displacement in the simulated plume. It can also be noted that the measured plumes are a fine scale feature and the sampling only lasted around half an hour, making it a challenging case to simulate yet illustrating a clear sampling of pollution plumes from power plant stacks, as a result of changing weather regime.

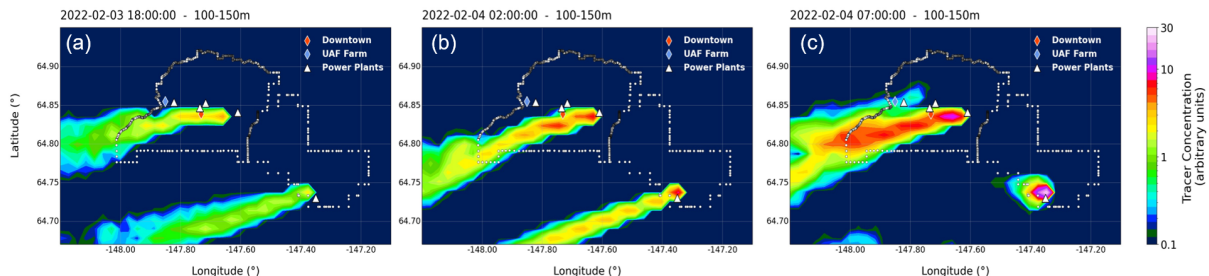


Figure 15. Spatial distribution of total power plant tracers simulated with FLEXPART-WRF between 100 - 150 m (arbitrary units), shown for a) before the Helikite flight at 18:00 LT on Feb. 3, b) during the Helikite flight at 2:00 LT on Feb. 4 and c) after the Helikite flight at 7:00 LT on Feb. 4. Power plants are indicated as white triangles, and the CTC and UAF Farm sites are indicated by red and blue diamonds, respectively.

8. Conclusions

The overarching theme of the ALPACA-2022 winter field experiment is to advance the understanding of the chemistry and microphysics of particulate matter and gasses in the unique conditions of the polar atmosphere during the winter (i.e., **when photochemistry is absent** and pollutant dispersion in stratified layers). However, inherent to the physical and chemical transformations of air pollution products is our ability to connect sources to receptors based on ground or airborne observational systems. This experiment fills this specific gap by providing critical observations to improve the model representation of the physical processes leading to extreme PBL states. This project supported experimental research to document surface radiative and turbulent fluxes, high resolution vertical profiling of thermodynamic variables and atmospheric composition of the PBL. The ensemble of datasets and observational platforms from this experiment aims to increase the synergy between experimental and modeling research. Thanks to the advanced observational platforms and tailored high-resolution modeling approaches, the meteorological processes in the lowest hundreds of meters above the ground and changes in atmospheric composition were characterized in detail during ALPACA-2022. However, despite the comprehensive multi-instrumental deployment, important limitations persist in achieving continuous and simultaneous sampling of the PBL's fine-scale structure and composition, particularly under harsh winter conditions, where the operation of platforms such as tethered balloons is constrained by logistical and environmental factors. As synthesis it was found that:

- a) Conditions of peak concentrations for gaseous and particulate pollutants were reached under weak synoptic forcing(**flows**) and strong surface temperature gradients, developing surface layers of pollutants 50 m thick (or even thinner). Such pollution layers were ventilated **because of** reduced temperature stratification (mainly from changes in the LW radiative heat balance) or because of intensified synoptic flows reaching down to the surface level.
- b) The shallow cold flows (SCFs) coming from the secondary valleys north and west of the larger Tanana Valley reduced surface stratification and can prevent pollution advection from downtown to suburban areas. Nevertheless, SCFs can still be a source of pollution and can promote downward mixing of plumes aloft (e.g., from power plant emissions).
- c) Even if SCFs cause heterogeneity in the surface wind fields in the Tanana Valley basin, the wind pattern above 100 m AGL is consistently dominated by an easterly-northeasterly circulation, forced by the **high-pressure ridge** extending between the Chukchi Peninsula and northern Alaska. This circulation drives a characteristic pattern in the transport of power plant plumes over the city with the west and southwesterly districts more exposed to possible deposition.

Overall, the ALPACA-2022 demonstrated significant synergy between different instrument platforms and modeling to study the dynamics and chemical composition of the PBL needed to bring deeper understanding to the air pollution problem in the harsh conditions of the winters of the Interior of Alaska. **Although this study is centered on Fairbanks, Alaska, the observed PBL structures, pollutant dispersion processes, and meteorological drivers are representative of conditions prevalent across Arctic and sub-Arctic regions. These results offer valuable insights into multi-scale interactions governing wintertime air pollution, establishing a framework that can inform understanding and modeling of cold-season atmospheric composition across the pan-Arctic domain.**

Acknowledgments.

The ALPACA project was initiated as a part of PACES under IGAC and with support of IASC. We thank University of Alaska Fairbanks and the College of Natural Science and

Mathematics and the Geophysical Institute for logistical support, and we thank Fairbanks for welcoming and engaging with this research.

G.J.F acknowledges support from NSF-grants 2117971, 2146929, and 2232282. K.S.L, B.d'A., B.B., S.B., N.B., H.D, E.D., A.I., J.-C.R., F.R., T.R, and B.T.-M. acknowledge support from the Agence National de Recherche (ANR) CASPA (Climate-relevant Aerosol Sources and Processes in the Arctic) project (grant no. ANR-21-CE01-0017), and the Institut polaire français Paul-Émile Victor (IPEV) (grant no. 1215) and CNRS-INSU programme LEFE (Les Enveloppes Fluides et l'Environnement) ALPACA-France projects. Computer modeling at LATMOS benefited from access to IDRIS HPC resources (GENCI allocations A013017141 and A015017141) and the IPSL mesoscale computing centre. R.P. and J.S. received funding from the Swiss National Science Foundation grant no. 200021_212101, and the Swiss Polar Institute Technogrant 2019. J.S. holds the Ingvar Kamprad chair for extreme environments research funded by Ferring Pharmaceuticals.

S.D., A.D., G.P., F.S. acknowledge support from the PRA ("Programma di Ricerche in Artico") 2019 programme (project "A-PAW") and from the ENI-CNR Joint Research Center "Aldo Pontremoli". W.R.S. and M.C.-M. acknowledge support from NSF grants 1927750 and 2109134.

J.M. acknowledge support from NSF grants 1927750 and 2029747. S.R.A. acknowledges support from the UK Natural Environment Research Council (grant ref. NE/W00609X/1). H. I., M. U. and Y. H. acknowledge funding support from the Arctic Challenge for Sustainability II (ArCS II; JPMXD1420318865), by MEXT, Japan and Effects of photosynthesis on the annual CO₂ budget of black spruce under extremely cold conditions, FY2019-22 Scientific Research (C) by MEXT, Japan.

Data Availability Statement.

Final data from the study will be available to the scientific community through the ALPACA data portal hosted by Arcticdata.io (<https://arcticdata.io/catalog/portals/ALPACA>).

REFERENCES

ADEC. Fairbanks North Star Borough (FNSB) Fine Particulate Matter (PM2.5) Serious State Implementation Plan, 2019: <https://dec.alaska.gov/air/anpms/communities/fbks-pm2-5-serious-sip/>(accessed: 03-03-2024).

AMAP, 2021. AMAP Assessment 2021: Impacts of Short-lived Climate Forcers on Arctic Climate, Air Quality, and Human Health. Arctic Monitoring and Assessment Programme (AMAP), Tromsø, Norway. x + 375pp

Ballinger, T. J., and Coauthors, 2023: Alaska Terrestrial and Marine Climate Trends, 1957–2021. *J. Climate*, 36, 4375–4391, <https://doi.org/10.1175/JCLI-D-22-0434.1>.

Barret B.,, P. Medina, S. Arnold, A. Baccarini, S. Bekki, N. Brett, M. Busetto, M. Cesler-Maloney, B. D'Anna, S. Decesari,, G. J. Fochesatto, J. Mao, G. Pappaccogli, R. Pohorsky, J. Savarino, J. Schmale, W. Simpson, F. Scoto and K. Law, 2024: Vertical profiles of trace gases (CO, O₃, NO, NO₂) in the Arctic wintertime boundary layer from low-cost sensors onboard a tethered balloon during ALPACA-2022. Submitted to *Atmospheric Meas. Tech.* June 2024.

Barrie, L., 1986: Arctic Air Pollution. Cambridge University Press, 328 pp

Bodurtha, F. T., 1952: An investigation of anticyclogenesis in Alaska. *J. Atmos. Sci.*, 9, 118–125

Bowling, S. A., T. Ohtake, and C. S. Benson, 1968: Winter Pressure Systems and Ice Fog in Fairbanks, Alaska. *J. Appl. Meteor. Climatol.*, 7, 961–968, [https://doi.org/10.1175/1520-0450\(1968\)007<0961:WPSAIF>2.0.CO;2](https://doi.org/10.1175/1520-0450(1968)007<0961:WPSAIF>2.0.CO;2).

Brett N., K.S. Law, S.R. Arnold, G. J. Fochesatto, J.C. Raut, T. Onishi, R. Gilliam, K. Fahey, D. Huff, G. Pouliot, B. Barret, E. Dieudonn{'e}, R. Pohorsky, J. Schmale, A. Baccarini, S. Bekki, G. Pappaccogli, F. Scoto, S. Decesari, A. Donateo, M. Cesler-Maloney, W. Simpson, B. D'Anna, B. Temime-Roussel, J. Savarino, S. Albertin, 1, J. Mao, P. F DeCarlo, V. Selimovic, and R. Yokelson (2024). Investigating processes influencing surface and power

plant air pollution in the stable wintertime Arctic boundary layer during ALPACA-2022.

Submitted to Atmospheric Chemistry and Physics.

Cassano, E. N., J. J. Cassano, and M. Nolan, 2011: Synoptic weather pattern controls on temperature in Alaska. *J. Geophys. Res.*, 116, D11108, doi:10.1029/2010JD015341.

Cesler-Maloney, M.; Simpson, W.R.; Miles, T.; Mao, J.; Law, K.S.; Roberts, T. J. 2022: Differences in Ozone and Particulate Matter between ground level and 20 m aloft are frequent during wintertime Surface-Based Temperature Inversions in Fairbanks, Alaska. *J. Geophys. Res. Atmospheres* 2022, 127(10), No.e2021JD036215.

Cohen, L., D. Helmig, W. Neff, A. Grachev, and C. Fairall, 2007: Boundary-layer dynamics and its influence on atmospheric chemistry at Summit, Greenland. *Atmos. Environ.*, 41, 5044-5060.

Chen, N., D. Guan, C. Jin, A. Wang, J. Wu, and F. Yuan, 2011: Influences of snow event on energy balance over temperate meadow in dormant season based on eddy covariance measurements. *J. Hydrol.*, 399 (1-2), 100–107.

Curry, J., 1983: On the Formation of Continental Polar Air. *J. Atmos. Sci.*, 40, 2278–2292, [https://doi.org/10.1175/1520-0469\(1983\)040<2278:OTFOCP>2.0.CO;2](https://doi.org/10.1175/1520-0469(1983)040<2278:OTFOCP>2.0.CO;2).

Curry, J., 1987: The Contribution of Radiative Cooling to the Formation of Cold-Core Anticyclones. *J. Atmos. Sci.*, 44, 2575–2592, [https://doi.org/10.1175/1520-0469\(1987\)044<2575:TCORCT>2.0.CO;2](https://doi.org/10.1175/1520-0469(1987)044<2575:TCORCT>2.0.CO;2).

Edwin G. S. and Mölders, N., 2020. Indoor and Outdoor Particulate Matter Exposure of Rural Interior Alaska Residents. *Open Journal of Air Pollution*, 9, 37-60. doi: 10.4236/ojap.2020.93004.

Fochesatto G. J., J. A. Mayfield, M. A. Gruber, D. Starkenburg, and J. Conner, 2015: Occurrence of shallow cold flows in the winter atmospheric boundary layer of interior of Alaska. *Meteorol. Atmos. Phys.* 127, 369–382 (2015). <https://doi.org/10.1007/s00703-013-0274-4>.

Hartl, L., C. Schmitt, T. Wong, D. A. Vas, L. Enterkin, and M. Stuefer, 2023: Long-Term Trends in Ice Fog Occurrence in the Fairbanks, Alaska, Region Based on Airport Observations. *J. Appl. Meteor. Climatol.*, 62, 1263–1278, <https://doi.org/10.1175/JAMC-D-22-0190.1>.

Hartmann, B., and G. Wendler (2005a), The significance of the 1976 Pacific climate shift in the climatology of Alaska, *J. Clim.*, 18, 4824–4839, doi:10.1175/JCLI3532.1.

Hartmann, B., and G. Wendler, (2005b): Climatology of the winter surface temperature inversion in Fairbanks, Alaska. Proc. Eighth Conf. on Polar Meteorology/16th Conf. on Climate Variability and Change, San Diego, CA, Amer. Meteor. Soc., JP2.26. [Available online at <https://ams.confex.com/ams/Annual2005/webprogram/Paper84504.html>]

Hersbach H, B. Bell, P. Berrisford, et al. 2020: The ERA5 global reanalysis. *Quarterly Journal of the Royal Meteorological Society*, 146:1999-2049.<https://doi.org/10.1002/qj.3803>

Hess, J. C., C. A. Scott, G. L. Hufford, and M. D. Fleming (2001), El Niño and its impact on fire weather conditions in Alaska, *Int. J. Wildland Fire*, 10, 1–13, doi:10.1071/WF01007

Huff, D. M., P. L. Joyce, G. J. Fochesatto, and W. R. Simpson, 2010: Deposition of dinitrogen pentaoxide, N₂O₅, to the snowpack at high latitudes. *Atmos. Chem. Phys. Discuss.*, 10, 25 329– 25 354.

Law, K. S., Stohl, A., Quinn, P. K., Brock, C. A., Burkhardt, J. F., Paris, J.-D., Ancellet, G., Singh, H. B., Roiger, A., Schlager, H., Dibb, J., Jacob, D. J., Arnold, S. R., Pelon, J. and Thomas, J. L.: Arctic Air Pollution: New Insights from POLARCAT-IPY, *Bull. Am. Meteorol.*

Soc., 95(12), 1873–1895, doi:10.1175/BAMS-D-13-00017.1, 2014.

Maillard J., J-C Raut, F. Ravetta, G. J. Fochesatto and K. Law, 2022: Modulation of boundary layer stability and the surface energy budget by a local flow in central Alaska. *Boundary-Layer Meteorology*, 185, , pp 395-414, <https://dx.doi.org/10.1007/s10546-022-00737-2>.

Maillard, J., Raut, J.-C., and Ravetta, F. 2024: Evaluation and development of surface layer scheme representation of temperature inversions over boreal forests in Arctic wintertime conditions, *Geosci. Model Dev.*, 17, 3303–3320, <https://doi.org/10.5194/gmd-17-3303-2024>, 2024.

Malingowski J., D. Atkinson, G. J. Fochesatto, J. Cherry and E. Stevens. 2014: An Observational Study of Radiation Temperature Inversions in Fairbanks, Alaska. *Polar Science*, 8, 1, 24-39.

Mantua, N. J. and Hare, S. R. (2002). The Pacific Decadal Oscillation. *Journal of Oceanography*. **58** (1): 35–44. doi:[10.1023/A:1015820616384](https://doi.org/10.1023/A:1015820616384). S2CID 5307916.

Mayfield J. and G. J. Fochesatto (2019). The Turbulence Regime of the Atmospheric Surface Layer in the Presence of Shallow Cold Drainage Flows. Application of Optical Laser Scintillometry. Chapter 5, Turbulence and Related Phenomena IntechOpen Rijeka, 2019. Edited by Dr. Regis Barille, Universite dAngers, France. doi = 10.5772/intechopen.80290, <https://doi.org/10.5772/intechopen.80290>.

Mayfield J. A. and G. J. Fochesatto. (2013). The Layered Structure of the winter Atmospheric Boundary Layer in the Interior of Alaska. *J. Appl. Met. Climatol.*, 52, 953-973.

Methven, J., S.R. Arnold, F.M. O'Connor, H. Barjat, K. Dewey, J. Kent, and N. Brough, (2003). Estimating Photochemically Produced Ozone Throughout a Domain Using Flight Data and a Lagrangian Model, *J. Geophys. Res.*, Vol. 108, No. D9, 4271

Mölders, N., and G. Kramm, 2010: A case study on wintertime inversions in Interior Alaska with WRF. *Atmos. Res.*, 95, 314-332.

Mölders, N., H. N. Q. Tran, P. Quinn, K. Sassen, G.E. Shaw and G. Kramm. 2011: Assessment of WRF/Chem to capture sub-Arctic boundary layer characteristics during low solar irradiation using radiosonde, SODAR, and station data. *Atmos. Pol. Res.* 2: 283-299.

Mölders N., H. N. Q. Tran, C. F. Cahill, K. Leelasakultum, T. T. Tran. 2012: Assessment of WRF/Chem PM2.5-forecasts using mobile and fixed location data from the Fairbanks, Alaska winter 2008/09 field campaign. *Atmos. Pol. Res.* doi: 10.5094/APR.2012.018.

Ohtake, T., and P. J. Huffman, 1969: Visual range in ice fog. *J. Appl. Meteor.*, 8, 499–501, [https://doi.org/10.1175/1520-0450\(1969\)008%3C0499:VRIIF%3E2.0.CO;2](https://doi.org/10.1175/1520-0450(1969)008%3C0499:VRIIF%3E2.0.CO;2).

Overland, J. E., and T. R. Hiester (1980), Development of a synoptic climatology for the northeast Gulf of Alaska, *J. Appl. Meteorol.*, 19, 1–14, doi:10.1175/1520-0450(1980)019<0001:DOASCF>2.0.CO;2.

Overland, J. E., J. M. Adams, and N. A. Bond (1999), Decadal variability of the Aleutian low and its relation to high-latitude circulation, *J. Clim.*, 12, 1542–1548, doi:10.1175/1520-0442(1999)012<1542:DVOTAL>2.0.CO;2.

Papineau, J. M. (2001), Wintertime temperature anomalies in Alaska correlated with ENSO and PDO, *Int. J. Climatol.*, 21, 1577–1592, doi:10.1002/joc.686.

Pohorsky R., A. Baccarini, N. Brett, B. Barret, E. Dieudonné, G. Pappaccogli, A. Donateo, S. Decesari, G. J. Fochesatto, S. Bekki, K. S. Law, W. Simpson, S. R. Arnold, J. Schmale. (2024). Observations of the layered structure of air pollution in the urban boundary layer during winter. Submitted to *Atmospheric Measurements Techniques* (August 2024).

Rodionov, S. N., J. E. Overland, and N. A. Bond (2005), The Aleutian low and winter

climatic conditions in the Bering Sea. Part I: Classification, *J. Clim.*, 18, 160–177, doi:10.1175/JCLI3253.1.

Schmale, J., Arnold, S. R., Law, K. S., Thorp, T., Anenberg, S., Simpson, W. R., et al. (2018). Local Arctic air pollution: A neglected but serious problem. *Earth's Future*, 6, 1385–1412. <https://doi.org/10.1029/2018EF000952>

Shulski, M., J. Walsh, E. Stevens, and R. Thoman (2010), Diagnosis of extended cold-season temperature anomalies in Alaska, *Mon. Weather Rev.*, 138, 453–462, doi:10.1175/2009MWR3039.1.

Simpson W.R., K. Law, J. Schmale, K. Pratt, S. Arnold, and J. Mao. IGAC-ALPACA (2018). Alaskan Layered Pollution And Chemical Analysis (ALPACA) White Paper, 2018:. <https://igacproject.org/publication/other-publications/alaskan-layered-pollution-and-chemical-analysis-alpaca-white-paper>.

Simpson W.R., J. Mao, G. J. Fochesatto, K. S. Law, P. F. DeCarlo, J. Schmale, K. A. Pratt, S. R. Arnold, J. Stutz, J. E. Dibb, J. M. Creamean, R. J. Weber, B. J. Williams, B. Alexander, L. Hu, R. J. Yokelson, M. Shiraiwa, S. Decesari, C. Anastasio, B. D'Anna, R. C. Gilliam, A. Nenes, J. M. St. Clair, B. Trost, J. H. Flynn, J. Savarino, L. D. Conner, N. Kettle, K. M. Heeringa, S. Albertin, A. Baccarini, B. Barret, M. A. Battaglia, S. Bekki, T.J. Brado, N. Brett, D. Brus, J. R. Campbell, M. Cesler-Malone, S. Cooperdock, K. Cysneiros de Carvalho, H. Delbarre, P. J. DeMott, C. J.S. Dennehy, E. Dieudonné, K. K. Dingilian, A. Donateo, K. M. Doulgeris, K. C. Edwards, K. Fahey, T. Fang, F. Guo, L. M. D. Heinlein, A. L. Holen, D. Huff, A. Ijaz, S. Johnson, S. Kapur, D. T. Ketcherside, E. Levin, E. Lill, A. R. Moon, T. Onishi, G. Pappaccogli, R. Perkins, R. Pohorsky, J-C Raut, F. Ravetta, T. Roberts, E. S. Robinson, F. Scoto, V. Selimovic, M. O. Sunday, B. Temime-Roussel, X. Tian, J. Wu, and Y. Yang (2024). Overview of the Alaskan Layered Pollution and Chemical Analysis (ALPACA) Field Experiment. *ACS ES&T Air* DOI: 10.1021/acsestaair.3c00076

Stone, R. S., 1997: Variations in western Arctic temperatures in response to cloud radiative

and synoptic-scale influences. *J. Geophys. Res.*, 102, 21769-21776. doi:10.1029/97JD01840.

Thomas, M. A., Devasthale, A., Tjernström, M. and Ekman, A. M. L., 2019: The relation between aerosol vertical distribution and temperature inversions in the Arctic in winter and spring. *Geophysical Research Letters*, 46, 2836–2845. <https://doi.org/10.1029/2018GL081624>